

Article

A High-Quality and Convenient Camera Calibration Method Using a Single Image

Xufang Qin, Xiaohua Xia *  and **Huatao Xiang**

Key Laboratory of Road Construction Technology and Equipment of MOE, Chang'an University, Xi'an 710064, China

* Correspondence: xhxia@chd.edu.cn

Abstract: Existing camera calibration methods using a single image have exhibited some limitations. These limitations include relying on large datasets, using inconveniently prepared calibration objects instead of commonly used planar patterns such as checkerboards, and requiring further improvement in accuracy. To address these issues, a high-quality and convenient camera calibration method is proposed, which only requires a single image of the commonly used planar checkerboard pattern. In the proposed method, a nonlinear objective function is derived by leveraging the linear distribution characteristics exhibited among corners. An algorithm based on enumeration theory is designed to minimize this function. It calibrates the first two radial distortion coefficients and principal points. The focal length and extrinsic parameters are linearly calibrated from the constraints provided by the linear projection model and the unit orthogonality of the rotation matrix. Additionally, a guideline is explored through theoretical analysis and numerical simulation to ensure calibration quality. The quality of the proposed method is evaluated by both simulated and real experiments, demonstrating its comparability with the well-known multi-image-based method and its superiority over advanced single-image-based methods.

Keywords: camera calibration; single image; linear distribution characteristics



Citation: Qin, X.; Xia, X.; Xiang, H. A High-Quality and Convenient Camera Calibration Method Using a Single Image. *Electronics* **2024**, *13*, 4361. <https://doi.org/10.3390/electronics13224361>

Academic Editor: Aryya Gangopadhyay

Received: 18 September 2024

Revised: 24 October 2024

Accepted: 5 November 2024

Published: 6 November 2024



Copyright: © 2024 by the authors. Licensee MDPI, Basel, Switzerland. This article is an open access article distributed under the terms and conditions of the Creative Commons Attribution (CC BY) license (<https://creativecommons.org/licenses/by/4.0/>).

1. Introduction

Camera calibration involves estimating internal parameters, extrinsic parameters, and distortion parameters from a mapping model between 3D points and their 2D projection points [1]. Within the field of 3D computer vision, camera calibration is crucial and finds extensive applications, including virtual reality [2], automatic driving [3], and optical measurement [4,5].

In accordance with the dimensionality of the calibration objects, camera calibration methods can be categorized. Self-calibration [6–8] is typically regarded as a 0D-object-based calibration approach because it dispenses with the need for a specific calibration object. Instead, it relies on acquiring multiple views of a static image scene through the camera, from which the camera parameters are subsequently estimated by identifying and matching reliable feature points. While the approach offers flexibility, its efficacy is contingent on the quality and quantity of matched feature points, which can introduce limitations. 1D-object-based calibration was investigated in Ref. [9]. Camera parameters could be derived by six or more views of a 1D object with one stationary point. The calibration object is easy to prepare, and self-occlusion will be avoided in a multi-camera setup. However, this approach necessitates multiple images and faces accuracy degradation when noise is existent. Two-dimensional-object-based calibration [10–12] can calibrate a camera by observing a planar pattern displayed at various orientations. The planar pattern is convenient to prepare, and the calibration accuracy is high. Nonetheless, the approach mandates capturing multiple images with diverse poses, which can be a drawback in certain scenarios. Three-dimensional-object-based calibration [13,14] is performed by looking at

an object with a well-defined geometry in 3D space. While this approach can yield accurate calibration results from a single view, it poses the difficulty of manufacturing a complex and expensive calibration object.

Given the respective advantages and disadvantages of the above calibration approaches, it will be more practical and highly efficient in applications if an accurate calibration method uses only a single image and an easily prepared calibration object. Currently, the work on single-image-based calibration involves three categories: Methods [15–17] that rely on models trained on large datasets to achieve calibration are in the first category. A learning-based method was proposed to accurately calibrate distortion parameters [15]. Subsequently, a deep learning model was introduced to obtain camera rotations, field of view, and distortion parameters [16]. Using the trained model for camera calibration yields reliable results. However, the process of creating the dataset for training the model is time-consuming.

The second category comprises approaches that achieve calibration using an image captured with a 3D calibration object [18–20]. A line-based camera calibration method was presented [19], which used three squares lying in distinct orientations. The two radial distortion coefficients were extracted via a non-linear optimization process by applying geometrical constraints along with separate model limitations. Once the distorted lines in the squares were corrected, the intrinsic parameters were subsequently computed using a homography matrix. Zhang et al. [20] separated the two radial distortion coefficients from the intrinsic parameters and independently solved for each parameter using a linear method based on an orthogonal checkerboard in two vertical planes. While this method achieves satisfactory calibration accuracy, the calibration objects are specially designed, which are inconvenient to prepare.

The last category comprises algorithms that achieve calibration using a single image with a 1D or 2D calibration object [21–26]. The extrinsic parameters and focal length could be calibrated based on five points viewed on a single image [21]. A camera calibration method was presented, which employed a single rectangular reference object [23]. Additionally, a robust camera calibration method [24] was proposed, predicated on noninfinite vanishing points observed within a single image containing a planar marker. These methods face challenges in achieving accurate camera calibration due to the lack of estimation of distortion parameters. The method presented in Ref. [25] employed a planar pattern for camera parameter estimation under the consideration of the lens distortion. The parameters were obtained by leveraging geometrical imaging principles, the radial distortion model, and linear equations. Using a single image of a planar speckle pattern displayed on a monitor, Genovese proposed a method to estimate camera calibration parameters. This method used digital image correlation for precise point matching and sequentially estimated the three radial distortion coefficients, principal points, focal length, and extrinsic parameters [26]. Although the calibration objects are easily prepared, further improvement of these methods is still required to not lose calibration quality.

To overcome the limitations of the previous single-image-based calibration methods, which require complex calibration objects or large datasets, two improvements are made in the proposed method. First, a planar checkboard, employed in the well-known Zhang's calibration method, is selected as a calibration board. Its widespread use in computer vision makes it easy to prepare. Second, only a single image of the calibration board is required to complete camera calibration. It eliminates the reliance on large datasets required in learning-based methods, which effectively reduces the work involved in calibration.

In response to the need for improved calibration accuracy observed in the previous single-image-based calibration methods, a high-quality calibration method is proposed. A decoupled calibration procedure is introduced to avoid coupling errors that affect calibration accuracy, whereby lens distortions are first corrected before proceeding to solve a linear model. To calibrate distortion parameters, an objective function is constructed based on an inverse distortion model and straight-line constraints from corner distributions. An optimization algorithm combining the least-squares fitting method with enumeration

theory is then presented to estimate distortion coefficients and principal points. Following this, a linear projection model is established between the corrected 2D corners and their corresponding 3D points, solving the camera's focal length and extrinsic parameters. Furthermore, the relationship between the state of the calibration board and calibration accuracy is analyzed. To ensure the quality of the calibration, the calibration guidelines for constraining the state of the calibration board is provided. The experimental results show that the calibration accuracy of the proposed method is comparable to that of the well-known multi-image-based Zhang's method and superior to that of the advanced single-image-based methods.

The contributions of this work are as follows:

- (i) High convenience: The proposed method only requires a single image of a commonly used planar checkboard, avoiding reliance on complex calibration objects or large datasets.
- (ii) High accuracy: An enhancement in calibration accuracy has been achieved through a designed decoupled calibration procedure, a proposed distortion parameter algorithm, and an exploration of the optimal state of the calibration board.
- (iii) High stability: The calibration guidelines effectively constrain the state of the calibration board, reducing fluctuations in the calibration results caused by changes in the state of the calibration board.

This paper is structured as follows: Section 2 introduces the imaging model, while Section 3 offers a comprehensive explanation of the proposed method. Section 4 is dedicated to the conduction and discussion of both simulated and real experiments. Lastly, the findings and conclusions are summarized in Section 5.

For clarity and reference, key notations used are listed in Table 1.

Table 1. Symbolic notation.

| Symbol | Description |
|---|--|
| $O_w X_w Y_w Z_w$ | The world coordinate frame |
| $O_c X_c Y_c Z_c$ | The camera coordinate frame |
| oxy | The image plane coordinate frame |
| P | A 3D point in $O_w X_w Y_w Z_w$ |
| p_u | An ideal projection 2D point without lens distortion |
| p_d | An actual 2D point based on the camera imaging model |
| $\begin{bmatrix} x_{dij} & y_{dij} \end{bmatrix}$ | A distorted corner of i th row and j th column |
| $\begin{bmatrix} u & v \end{bmatrix}$ | Coordinates of the principal points in oxy |
| $\begin{bmatrix} R & t \end{bmatrix}$ | The rotation and translation that relates $O_w X_w Y_w Z_w$ to $O_c X_c Y_c Z_c$ |
| α, β | Focal length |
| k_1, k_2 | Radial distortion coefficients |
| W, H | The width and height of an image |
| m, n | The number of rows and columns of corners |
| NC | The number of corners in an image |
| FL | Fullness level of corners in an image |
| HL, VL | Horizontal and vertical symmetry level of corners in an image |
| θ_1, θ_2 | Rotation angles around axis X_c and Y_c |
| $E_\alpha, E_\beta, E_\mu, E_v$ | Relative errors of α, β, u , and v |
| Re | Mean squared reprojection error |

2. Imaging Model

A pure linear projection cannot describe the imaging process of a camera well, as real lenses create distortion [27]. As depicted in Figure 1, a camera imaging model that combines lens distortion with the pin-hole model is required.

Based on the principle of pin-hole imaging, the linear relationship between a 3D point P and an ideal projection 2D point p_u is given by

$$s\tilde{\mathbf{p}}_u = A\tilde{\mathbf{P}}, \text{ with } A = \begin{bmatrix} \alpha & \gamma & v \\ 0 & \beta & u \\ 0 & 0 & 1 \end{bmatrix} \text{ and } T = [R \ t], \quad (1)$$

where T is the extrinsic matrix, γ is called the skew of the two image axes, A is the intrinsic matrix, s represents the scale factor, and $\tilde{\mathbf{P}}$ and $\tilde{\mathbf{p}}_u$ are the homogeneous coordinates of \mathbf{P} and \mathbf{p}_u , respectively.

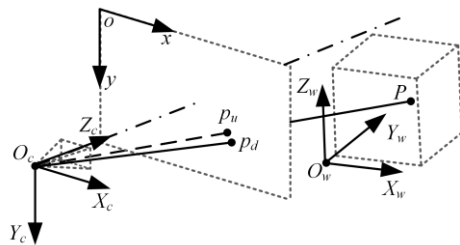


Figure 1. Camera imaging model.

In reality, the actual projection point of P is p_d due to lens distortion. Lens distortion is commonly decomposed into radial, decentering, and prism components. For most vision systems, radial distortion is sufficient to achieve high-accuracy measurements, as the impact of other distortion components on accuracy is insignificant. Additionally, in this paper, the initially extracted projection point is p_d , while p_u remains unknown. Thus, the inverse distortion model [19] is introduced to describe the relationship between p_u and p_d .

$$\mathbf{p}_u = \mathbf{p}_d + \Delta\mathbf{p}_d(k_1r_d^2 + k_2r_d^4), \quad (2)$$

where k_1 and k_2 are the coefficients of the radial distortion, $\Delta\mathbf{p}_d = \mathbf{p}_d - cc$ represents the displacement from \mathbf{p}_d to cc , $r_d = \|\mathbf{p}_d - cc\|_2$ is the Euclidean distance between \mathbf{p}_d and cc , and cc is equal to $[u \ v]^T$.

3. Methodology

The calibration method is composed of three steps. Estimating distortion parameters to achieve image distortion correction is the first step. The purpose of this step is to eliminate the effect of lens distortion, allowing an accurate representation of the imaging process through a purely linear projection. Estimating focal length and extrinsic parameters linearly is involved in the next step. To ensure the calibration quality, the last step is to explore guidance in the calibration procedure.

3.1. Distortion Correction

In this part, the purpose is to obtain the undistorted checkboard image composed of m horizontal straight lines (l) and n vertical straight lines (p), as shown in Figure 2. These straight lines will curve to a certain extent due to lens distortion. Therefore, by correcting the curved lines to straight lines, distortion coefficients and principal points can be solved.

Let the undistorted corner of i th row and j th column be $\mathbf{p}_{uij} = [x_{uij} \ y_{uij}]^T$ in oxy . Equation (3) can be obtained by least-squares linear fitting of n corners in i th row.

$$\hat{l} : \left\{ y_{uij} = \hat{a}_i x_{uij} + \hat{b}_i \mid j = 1..n \right\}, \quad (3)$$

where \hat{a}_i and \hat{b}_i are the slope and the intercept for the i th straight line. Accordingly, m corners in j th column can also be linearly fitted. To avoid an infinite slope, the fitted line can be expressed as

$$\hat{p} : \left\{ x_{uij} = \hat{a}_j y_{uij} + \hat{b}_j \mid i = 1..m \right\}, \quad (4)$$

where \hat{a}_j and \hat{b}_j are the reciprocal of the slope and the negative intercept divided by the slope for the j th straight line.

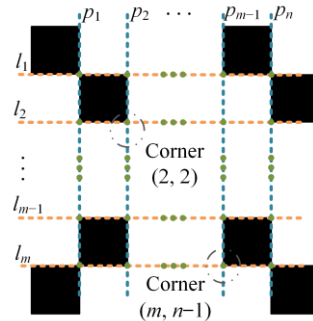


Figure 2. The image of a checkboard without distortion.

The radial distortion coefficients and the principal points are obtained via minimizing the following objective function:

$$\sum_{i=1}^m \sum_{j=1}^n \left\| y_{uij} - \hat{l}_i(\hat{a}_i, \hat{b}_i, x_{uij}) \right\|_2 + \sum_{j=1}^n \sum_{i=1}^m \left\| x_{uij} - \hat{p}_j(\hat{a}_j, \hat{b}_j, y_{uij}) \right\|_2' \quad (5)$$

with

$$\begin{bmatrix} x_{uij} \\ y_{uij} \end{bmatrix} = \mathbf{p}_{uij} = \mathbf{p}_{dij} + \Delta \mathbf{p}_{dij} (k_1 r_{dij}^2 + k_2 r_{dij}^4). \quad (6)$$

The result of Equation (5) means the fitting error. A minimal result is expected. Minimizing Equation (5) is a nonlinear minimization problem. To solve the problem, the algorithm for estimating radial distortion coefficients and principal points based on enumeration theory is designed. The flow of the designed algorithm is shown in Algorithm 1. The output parameters solved by Algorithm 1 are the radial distortion coefficients k_1 and k_2 and the principal points u and v . Subsequently, the distorted image can be corrected by Equation (2).

Algorithm 1: Distortion parameter estimation based on enumeration theory

```

Input:  $\{p_{dij} | i = 1..m, j = 1..n\}, m, n, \delta p_c$ , resolution ( $W$  pixels  $\times$   $H$  pixels)
Output:  $u_{0\_p}, v_{0\_p}, k_{1\_p}, k_{2\_p}$ 
Initialization :  $u_{0\min}, u_{0\max}, v_{0\min}, v_{0\max}, k_{1\min}, k_{1\max}, k_{2\min}, k_{2\max}, \delta u, \delta v, \delta k_1, \delta k_2, \text{err} = 1 \times 10^{10}$ 
for  $u \leftarrow u_{0\min}$  to  $u_{0\max}$  step  $\delta u$  do
    for  $v \leftarrow v_{0\min}$  to  $v_{0\max}$  step  $\delta v$  do
        for  $k_1 \leftarrow k_{1\min}$  to  $k_{1\max}$  step  $\delta k_1$  do
            for  $k_2 \leftarrow k_{2\min}$  to  $k_{2\max}$  step  $\delta k_2$  do
                compute (6)  $\rightarrow E$ 
                if  $E < \text{err}$ 
                     $\text{err} \leftarrow E; k_{1\_p} \leftarrow k_1; k_{2\_p} \leftarrow k_2; u_{0\_p} \leftarrow u; v_{0\_p} \leftarrow v$ 
                end if
            end for
        end for
    end for
end for

```

The key parameters involved in Algorithm 1 are introduced in detail in the following. In the input, δp_c represents the component of the uncertainty of the distortion-corrected point p_c due to the uncertainties of u, v, k_1 , and k_2 . The point p_c is equal to $[x_u \ y_u]^T$. Let us denote the contribution of the uncertainties of u, v, k_1 , and k_2 to the uncertainty of x_u as $\delta x_{u_k_1}, \delta x_{u_k_2}, \delta x_{u_u}$, and δx_{u_v} , and the contribution of them to the uncertainty of y_u as

$\delta y_{u_k_1}$, $\delta y_{u_k_2}$, δy_{u_u} , and δy_{u_v} . In the initialization, the determination of each parameter is as follows: Considering that principal points are usually located around the center of the image, $u_{0\max}$, $u_{0\min}$, $v_{0\max}$, and $v_{0\min}$ are equal to $0.5 W + 0.5 aW$, $0.5 W - 0.5 aW$, $0.5 H + 0.5 aH$, and $0.5 H - 0.5 aH$, separately. The value of a can be tentatively taken as 0.5. When u_{0_p} or v_{0_p} is located at the search boundary, the value of a should be increased. The steps to determine $k_{1\min}$, $k_{1\max}$, $k_{2\min}$, $k_{2\max}$, δu , δv , δk_1 , and δk_2 are as follows:

The lens distortion caused by k_1 is defined as $[b_1 W \ b_2 H]^T$, the value of u is represented by $b_3 W$, and the value of v is set as $b_4 H$. Generally, the lens distortion generated by k_1 is greater than that generated by k_2 . Thus, the maximum lens distortion generated by k_2 is equal to $[b_1 W \ b_2 H]^T$. The maximum distortion occurs at the position where p_d is farthest from the principal points, that is, $p_d = [x_d \ y_d]^T = [W \ H]^T$. Equation (7) can be obtained based on Equation (2) by substituting the set p_d , u , v , lens distortion caused by k_1 , and maximum lens distortion caused by k_2 .

$$\begin{cases} k_{1\min} = \frac{-b_1}{(W^2(1-b_3)^2 + H^2(1-b_4)^2)(1-b_3)}, & k_{1\max} = \frac{b_1}{(W^2(1-b_3)^2 + H^2(1-b_4)^2)(1-b_3)} \\ k_{2\min} = \frac{-b_1}{(W^2(1-b_3)^2 + H^2(1-b_4)^2)^2(1-b_3)}, & k_{2\max} = \frac{b_1}{(W^2(1-b_3)^2 + H^2(1-b_4)^2)^2(1-b_3)} \end{cases} . \quad (7)$$

After giving the values of b_1 , b_2 , b_3 , and b_4 to 0.125, 0.125, 0.5, and 0.5, we can obtain the following:

$$\begin{cases} k_{1\min} = \frac{-1}{W^2+H^2}, & k_{1\max} = \frac{1}{W^2+H^2} \\ k_{2\min} = \frac{-4}{(W^2+H^2)^2}, & k_{2\max} = \frac{4}{(W^2+H^2)^2} \end{cases} . \quad (8)$$

The lens distortion is shown in Figure 3. The distortion shown in Figure 3 is sufficient for the usual industrial camera because the lens distortion of the usual industrial camera is not severe. That is to say, the search intervals of k_1 and k_2 determined by Equation (8) are adequate for the usual industrial camera. Worthy of mention is that if k_{1_p} or k_{2_p} is located at the search boundary, the values of b_1 , b_2 , b_3 , and b_4 should be adjusted and the search intervals of k_1 and k_2 calculated by Equation (7).

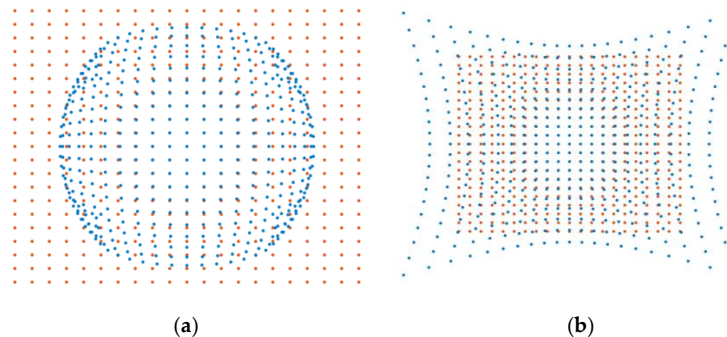


Figure 3. Lens distortion. The red dots represent undistorted points, and the blue dots represent distorted points. (a) Barrel distortion generated by $k_{1\min}$ and $k_{2\min}$; (b) pillow distortion generated by $k_{1\max}$ and $k_{2\max}$.

Next, the determination of δu , δv , δk_1 , and δk_2 is introduced. The values of δu , δv , δk_1 , and δk_2 can affect uncertainties of u , v , k_1 , and k_2 , which impact the distortion correction accuracy. Let us suppose that the uncertainty of u , v , k_1 , and k_2 is equivalent to δu , δv , δk_1 , and δk_2 , respectively. The relationship between δu , δv , δk_1 , and δk_2 and the accuracy of the distortion correction is expressed by Equation (9) under the condition of only considering $\delta x_{u_k_1}$, $\delta x_{u_k_2}$, δx_{u_u} , δx_{u_v} , $\delta y_{u_k_1}$, $\delta y_{u_k_2}$, δy_{u_u} , and δy_{u_v} .

$$\begin{cases} \delta x_u = \sqrt{(\delta x_{u_k_1})^2 + (\delta x_{u_k_2})^2 + (\delta x_{u_u})^2 + (\delta x_{u_v})^2} \\ \delta y_u = \sqrt{(\delta y_{u_k_1})^2 + (\delta y_{u_k_2})^2 + (\delta y_{u_u})^2 + (\delta y_{u_v})^2} \end{cases} , \quad (9)$$

where

$$\left\{ \begin{array}{l} \delta x_{u_k_1} = \sqrt{\left(\frac{\partial x_u}{\partial k_1} \delta k_1\right)^2}, \delta x_{u_k_2} = \sqrt{\left(\frac{\partial x_u}{\partial k_2} \delta k_2\right)^2} \\ \delta x_{u_u} = \sqrt{\left(\frac{\partial x_u}{\partial u} \delta u\right)^2}, \delta x_{u_v} = \sqrt{\left(\frac{\partial x_u}{\partial v} \delta v\right)^2} \\ \delta y_{u_k_1} = \sqrt{\left(\frac{\partial y_u}{\partial k_1} \delta k_1\right)^2}, \delta y_{u_k_2} = \sqrt{\left(\frac{\partial y_u}{\partial k_2} \delta k_2\right)^2} \\ \delta y_{u_u} = \sqrt{\left(\frac{\partial y_u}{\partial u} \delta u\right)^2}, \delta y_{u_v} = \sqrt{\left(\frac{\partial y_u}{\partial v} \delta v\right)^2} \\ \frac{\partial x_u}{\partial k_1} = (x_d - u)r_d^2, \frac{\partial x_u}{\partial u} = -(k_1 r_d^2 + k_2 r_d^4) - 2(x_d - u)^2(k_1 + 2k_2 r_d^2) \\ \frac{\partial x_u}{\partial k_2} = (x_d - u)r_d^4, \frac{\partial x_u}{\partial v} = -2(x_d - u)(y_d - v)(k_1 + 2k_2 r_d^2) \\ \frac{\partial y_u}{\partial k_1} = (y_d - v)r_d^2, \frac{\partial y_u}{\partial u} = -2(x_d - u)(y_d - v)(k_1 + 2k_2 r_d^2) \\ \frac{\partial y_u}{\partial k_2} = (y_d - v)r_d^4, \frac{\partial y_u}{\partial v} = -(k_1 r_d^2 + k_2 r_d^4) - 2(y_d - v)^2(k_1 + 2k_2 r_d^2) \end{array} \right. . \quad (10)$$

From Equation (9), when δu , δv , δk_1 , and δk_2 are constant, the farther p_d is from cc , the greater δx_u and δy_u are, and the worse the distortion correction accuracy is. In other words, p_d furthest from cc in an image is corrected with the lowest accuracy. In addition, when p_d is fixed, the smaller δu , δv , δk_1 , and δk_2 are, the smaller δx_u and δy_u are, the better the distortion correction accuracy is, and the longer the calculation time is. Considering the calculation time, p_d farthest from cc is selected to calculate the maximum δu , δv , δk_1 , and δk_2 that can meet the requirement of the distortion correction accuracy. Assuming that the lens distortion is $[b_5W \ b_6H]^T$, Equation (11) can be obtained.

$$\left\{ \begin{array}{l} x_d - u = (1 - b_3)W, y_d - v = (1 - b_4)H \\ |x_u - x_d| = b_5W, |y_u - y_d| = b_6H \end{array} \right. . \quad (11)$$

Joining Equations (10) and (11) gives

$$\left\{ \begin{array}{l} \delta k_1 = \min\{\delta k_{1_x}, \delta k_{1_y}\}, \delta k_2 = \min\{\delta k_{2_x}, \delta k_{2_y}\} \\ \delta u = \min\{\delta u_{_x}, \delta u_{_y}\}, \delta v = \min\{\delta v_{_x}, \delta v_{_y}\} \end{array} \right. . \quad (12)$$

where

$$\left\{ \begin{array}{l} \delta k_{1_x} = \frac{\delta x_{u_k_1}}{(1-b_3)W((1-b_3)^2W^2+(1-b_4)^2H^2)} \\ \delta k_{1_y} = \frac{\delta y_{u_k_1}}{(1-b_3)H((1-b_3)^2W^2+(1-b_4)^2H^2)} \\ \delta k_{2_x} = \frac{\delta x_{u_k_2}}{(1-b_3)W((1-b_3)^2W^2+(1-b_4)^2H^2)} \\ \delta k_{2_y} = \frac{\delta y_{u_k_2}}{(1-b_3)H((1-b_3)^2W^2+(1-b_4)^2H^2)} \\ \delta u_{_x} = \left((1-b_3)^2W^2 + (1-b_4)^2H^2 \right) \delta x_{u_u} \left(\begin{array}{l} \left(\frac{b_5}{1-b_3} \right) \left((1-b_3)^2W^2 + (1-b_4)^2H^2 \right) - 2(1-b_3)^2 \\ W^2 \left(\frac{-b_6}{1-b_4} + k_2 \left((1-b_3)^2W^2 + (1-b_4)^2H^2 \right)^2 \right) \end{array} \right)^{-1} \\ \delta u_{_y} = \frac{((1-b_3)^2W^2 + (1-b_4)^2H^2)\delta y_{u_u}}{-2(1-b_3)(1-b_4)\left(\frac{-b_6}{1-b_4} + k_2 \left((1-b_3)^2W^2 + (1-b_4)^2H^2 \right)^2 \right)} \\ \delta v_{_x} = \frac{((1-b_3)^2W^2 + (1-b_4)^2H^2)\delta x_{u_v}}{-2(1-b_3)(1-b_4)\left(\frac{-b_6}{1-b_4} + k_2 \left((1-b_3)^2W^2 + (1-b_4)^2H^2 \right)^2 \right)} \\ \delta v_{_y} = \left((1-b_3)^2W^2 + (1-b_4)^2H^2 \right) \delta y_{u_v} \left(\begin{array}{l} \left(\frac{b_5}{1-b_3} \right) \left((1-b_3)^2W^2 + (1-b_4)^2H^2 \right) - 2(1-b_3)^2 \\ H^2 \left(\frac{-b_6}{1-b_4} + k_2 \left((1-b_3)^2W^2 + (1-b_4)^2H^2 \right)^2 \right) \end{array} \right)^{-1} \end{array} \right. . \quad (13)$$

By substituting $b_5 = b_6 = 2b_1 = 0.25$, $b_3 = b_4 = 0.5$, and Equation (8) into Equation (12), Equation (12) is simplified as Equation (14).

$$\begin{cases} \delta k_1 = \min \left\{ \frac{8\delta x_{u,k_1}}{W(W^2+H^2)}, \frac{8\delta y_{u,k_1}}{H(W^2+H^2)} \right\} \\ \delta k_2 = \min \left\{ \frac{2\delta x_{u,k_2}}{W(0.25W^2+0.25H^2)^2}, \frac{2\delta y_{u,k_2}}{H(0.25W^2+0.25H^2)^2} \right\} \\ \delta u = \min \left\{ \frac{2\delta x_{u,u}(W^2+H^2)}{2W^2+H^2}, \frac{\delta y_{u,u}(W^2+H^2)}{0.5WH} \right\} \\ \delta v = \min \left\{ \frac{\delta x_{u,v}(W^2+H^2)}{0.5WH}, \frac{2\delta y_{u,v}(W^2+H^2)}{W^2+2H^2} \right\} \end{cases}. \quad (14)$$

Using Equation (14), δu , δv , δk_1 , and δk_2 are determined, which are suitable for the usual industrial camera. Notably, when the search intervals of k_1 and k_2 are given by Equation (7), δu , δv , δk_1 , and δk_2 should be calculated by using Equation (13).

3.2. Remaining Parameters Estimation

In general, γ can be supposed as 0 because current camera manufacturing technology can guarantee this [10]. The remaining parameters to be calibrated contain α , β , \mathbf{R} , and \mathbf{t} .

Let the corner of the i th row and j th column be $\mathbf{P}_{ij} = [X_{ij} \ Y_{ij} \ 0]^T$ in $O_w X_w Y_w Z_w$, and denote the i th column of the rotation matrix \mathbf{R} as \mathbf{r}_i . From the linear imaging process of the pin-hole model in Figure 1, Equation (1) can be rewritten as

$$\begin{bmatrix} x_{uij} \\ y_{uij} \\ 1 \end{bmatrix} = \mathbf{H} \begin{bmatrix} X_{ij} \\ Y_{ij} \\ 1 \end{bmatrix}, \quad \text{with } \mathbf{H} = [\mathbf{h}_1 \ \mathbf{h}_2 \ \mathbf{h}_3] = \lambda \begin{bmatrix} \alpha & 0 & u \\ 0 & \beta & v \\ 0 & 0 & 1 \end{bmatrix} [\mathbf{r}_1 \ \mathbf{r}_2 \ \mathbf{t}], \quad (15)$$

where \mathbf{h}_i represents the i th column of the homologous matrix \mathbf{H} , $\lambda = 1/\|A^{-1}\mathbf{h}_1\| = 1/\|A^{-1}\mathbf{h}_2\|$ means an arbitrary scalar. The matrix \mathbf{C} is constructed as shown in (16).

$$\mathbf{C} = \begin{bmatrix} 1 & 0 & -u \\ 0 & 1 & -v \\ 0 & 0 & 1 \end{bmatrix}. \quad (16)$$

The matrix obtained by multiplying \mathbf{C} by \mathbf{H} is denoted by $\mathbf{Q} = [\mathbf{q}_1 \ \mathbf{q}_2 \ \mathbf{q}_3]$. Equation (17) can be obtained together with Equations (15) and (16).

$$[\mathbf{q}_1 \ \mathbf{q}_2 \ \mathbf{q}_3] = \lambda \mathbf{K} [\mathbf{r}_1 \ \mathbf{r}_2 \ \mathbf{t}], \quad \text{with } \mathbf{K} = \begin{bmatrix} \alpha & 0 & 0 \\ 0 & \beta & 0 \\ 0 & 0 & 1 \end{bmatrix}. \quad (17)$$

By leveraging the fact that \mathbf{r}_1 and \mathbf{r}_2 are orthonormal, two basic constraints can be expressed as

$$\begin{aligned} \mathbf{q}_1^T \mathbf{K}^{-T} \mathbf{K}^{-1} \mathbf{q}_2 &= 0, \\ \mathbf{q}_1^T \mathbf{K}^{-T} \mathbf{K}^{-1} \mathbf{q}_1 &= \mathbf{q}_2^T \mathbf{K}^{-T} \mathbf{K}^{-1} \mathbf{q}_2. \end{aligned} \quad (18)$$

Thus, α and β can be obtained by solving Equation (18). The extrinsic parameters for the image are readily computed, as A is known at this moment.

$$\mathbf{r}_1 = \lambda \mathbf{A}^{-1} \mathbf{h}_1, \mathbf{r}_2 = \lambda \mathbf{A}^{-1} \mathbf{h}_2, \mathbf{r}_3 = \mathbf{r}_1 \times \mathbf{r}_2, \mathbf{t} = \lambda \mathbf{A}^{-1} \mathbf{h}_3. \quad (19)$$

3.3. The Guidance in the Calibration Procedure

The proposed method has two main limitations: (i) $O_w X_w Y_w Z_w$ cannot be parallel to $O_c X_c Y_c Z_c$. Otherwise, the results of the proposed method will fail because the singular matrix will appear in Section 3.2. (ii) The farther the corner in the image is from the principal points, the more pronounced the distortion becomes, and the more accurately the distortion parameters can be estimated. Moreover, the lens distortion is approximately

symmetric about the image midline. Additionally, the results of least-squares linear fitting are tightly correlated with the distribution and number of corners in the image. The corners in the image should be evenly distributed throughout the image and in sufficient numbers. Otherwise, the quality of the proposed method will decline.

To deal with the limitations and ensure the calibration quality of the proposed method, the guidance in the calibration procedure is presented. The guidance requires that the state of the calibration object is constrained during the calibration procedure and aims to clarify what calibration object state can guarantee calibration quality. Since the true camera parameters and the functional relationship between the calibration object state and the calibration quality are unknown, the numerical simulation analysis is selected to explore the guidance. The state of the calibration object involves the extrinsic parameters, the number of corners, and the size of the checkerboard. The extrinsic parameters contain the translation along axis Z_c (t_3), the translation along axis Y_c (t_2), the translation along axis X_c (t_1), the rotation angle around axis Z_c (θ_3), the rotation angle around axis Y_c (θ_2), and the rotation angle around axis X_c (θ_1).

First, the factors, which affect calibration quality originating from the calibration object state, are determined. The number of corners and the size of the checkerboard in a calibration object affects the factor named the number of corners in the image (NC). The values of θ_1 and θ_2 affect the factor named the inclination angle of the checkerboard in the image. Using the checkerboard in the image when $O_wX_wY_wZ_w$ is parallel to $O_cX_cY_cZ_c$ as a reference, the larger values of θ_1 and θ_2 are, the greater the inclination angle is. Let the distorted corner of the i th row and j th column be $p_{dij} = [x_{dij} \ y_{dij}]^T$ in oxy . The factor named the fullness level of corners in the image (FL) is affected by the value of t_3 and the size of the checkerboard, which is evaluated by Equation (20). The value of FL is positively correlated with the fullness level of corners in the image.

$$FL = 0.25W^{-1}H^{-1}(x_{d11} - x_{d1n} + x_{dm1} - x_{dmn})(y_{d11} - y_{dm1} + y_{d1n} - y_{dmn}). \quad (20)$$

The values of t_2 , t_1 , and θ_3 affect the factor named the symmetry level of corners in the image. The symmetry level is quantified by Equation (21), which is divided into the horizontal symmetry level (HL) and the vertical symmetry level (VL). The larger the value of HL, the more asymmetric the distribution of corners in the image with respect to the image horizontal midline. The larger the value of VL, the more asymmetric the distribution of corners in the image with respect to the image vertical midline.

$$\begin{aligned} HL &= \left| (y_{d11} - v)(v - y_{dm1})^{-1} - 1 \right| + \left| (y_{d1n} - v)(v - y_{dmn})^{-1} - 1 \right|, \\ VL &= \left| (x_{d11} - u)(u - x_{d1n})^{-1} - 1 \right| + \left| (x_{dm1} - u)(u - x_{dmn})^{-1} - 1 \right|. \end{aligned} \quad (21)$$

Subsequently, the specific numerical simulation step is set to explore the relationship between the accuracy of the proposed method and the state of a calibration object.

- (i) Initialization. Set the values of the state of the calibration object, camera internal parameters, lens distortion parameters, and the noise level of corners.
- (ii) Single-factor numerical simulation. A single factor is selected for adjustment, and the other factors are held constant. The state of the calibration object is then changed. Combined with the set values in step (i), the accuracy of the proposed method is evaluated under this state of the calibration object. The factor is changed several times, and the relationship between the factor and the calibration quality is obtained.
- (iii) Repetition. Step (ii) is repeated until the relationship between all factors and the calibration quality is obtained.

The camera intrinsic parameters and lens distortion parameters are randomly set, as shown in Table 2. Angle vector r and translation vector t are used to describe the camera extrinsic parameters. We set $r = [3^\circ, 3^\circ, 0^\circ]$ and $t = [-153 \text{ mm}, -107 \text{ mm}, 620 \text{ mm}]$. The 88 corners on the planar pattern are evenly distributed, with a size of the checkerboard of

30 mm. The distribution of corners in the image shown in Figure 4 is obtained. To prevent the simulated corners from exceeding the field of view, the ranges of θ_1 , θ_2 , and θ_3 are set to $(-25^\circ, 85^\circ)$, $(-85^\circ, 25^\circ)$, and $(-5^\circ, 5^\circ)$.

Table 2. Parameters for simulation.

| Parameter | Resolution | α (Pixel) | β (Pixel) | u (Pixel) | v (Pixel) | k_1 (Pixel $^{-2}$) | k_2 (Pixel $^{-4}$) |
|-----------|--------------------|------------------|-----------------|-------------|-------------|------------------------|------------------------|
| Truth | 1600×1200 | 2800 | 2800 | 810 | 605 | -5.0×10^{-8} | 2.0×10^{-14} |

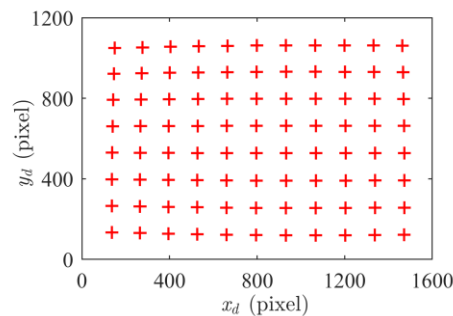


Figure 4. Simulated corners.

The relative errors of α , β , u , and v are used to evaluate the calibration quality, which is defined as Equation (22).

$$E_\alpha = \frac{|\alpha - \tilde{\alpha}|}{\tilde{\alpha}}, E_\beta = \frac{|\beta - \tilde{\beta}|}{\tilde{\beta}}, E_u = \frac{|u - \tilde{u}|}{\tilde{u}}, E_v = \frac{|v - \tilde{v}|}{\tilde{v}}, \quad (22)$$

where α , β , u , and v are the estimated intrinsic parameters, and $\tilde{\alpha}$, $\tilde{\beta}$, \tilde{u} , and \tilde{v} are the ground truth.

(I) The number of corners

By adjusting the number of corners on the planar pattern and the size of the checkerboard, the number of corners in the image is adjusted on the basis of Figure 4. The number of corners in the image after adjustment is shown in Figure 5. Three steps are involved in the experiment: The first step is that Gaussian noise with a mean of 0 and a standard deviation of 0.2 pixels is added to the simulated corners in each image to simulate the corner extraction error in the real calibration procedure. The second step is that E_α , E_β , E_u , and E_v of each image are calculated. The last step is to repeat step 1 and step 2 twenty times to avoid the contingency of the experimental results.

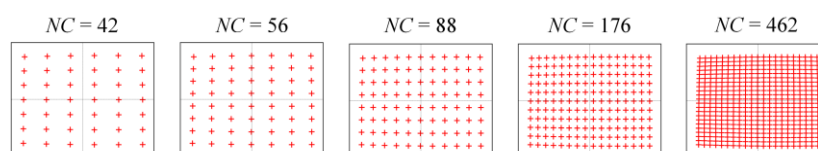


Figure 5. The number of corners in the image.

The results shown in Figure 6 illustrate that the calibration quality is improved with the increase of the number of corners in the image. Furthermore, E_α , E_β , E_u , and E_v can be kept below 1.5% if the number of corners in the image is above 56. It suggests that the greater number of corners in the image can ensure calibration quality, and the strategy of increasing corners in the image is favorable for improving the calibration quality.

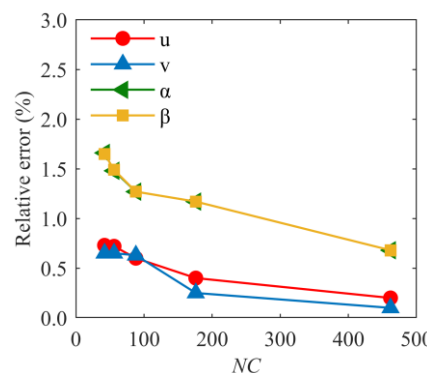


Figure 6. The relationship between the number of corners in the image and the calibration quality.

(II) The fullness level

To simulate the changes in the fullness level of corners in the image, t_3 is varied. As shown in Figure 7, the fullness level of corners in the image, calculated by Equation (20), increases or decreases after adjustment, starting from Figure 4.

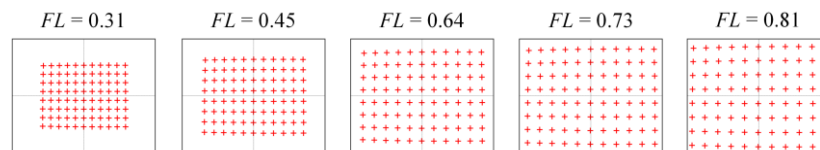


Figure 7. The fullness level of corners in the image.

Experiments are conducted according to the experimental step described in part (I) of Section 3.3. In Figure 8, the relationship between the fullness level and the calibration quality is displayed. As the fullness level of corners in the image increases, the calibration quality improves. It can be seen that the fullness level has little effect on the calibration quality when it is below 0.64. The reason is that the distortion coefficients cannot be effectively estimated. When FL exceeds 0.64, its increase will rapidly improve the calibration quality. Therefore, greater FL can improve calibration quality.

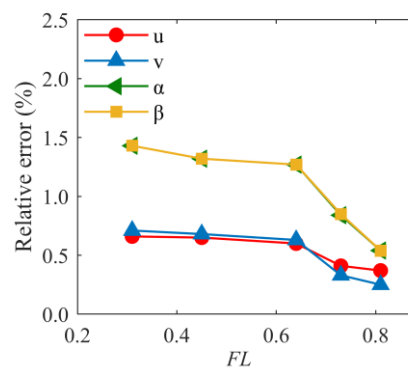


Figure 8. The relationship between the fullness level of corners in the image and the calibration quality.

(III) The symmetry level

Based on Figure 4, the change of the horizontal symmetry level of corners in the image is achieved by adjusting t_2 , and the change of the vertical symmetry level of corners in the image is obtained by adjusting t_1 . The symmetry level of corners in the image, quantified using Equation (21), is shown to change in Figure 9.

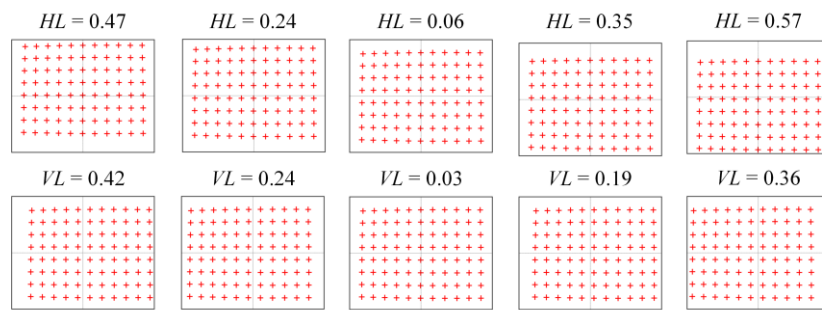


Figure 9. The symmetry level of corners in the image.

The experiments are conducted based on the experimental steps described in part (I) of Section 3.3, and the experimental results are shown in Figure 10. The calibration quality decreases with the increase of HL and VL . The value of θ_3 should be kept as small as possible, as its increase can rapidly increase HL and VL , thereby decreasing the symmetrical distribution of corners in the image. The effective way to improve calibration quality is by increasing the symmetrical distribution of corners in the image.

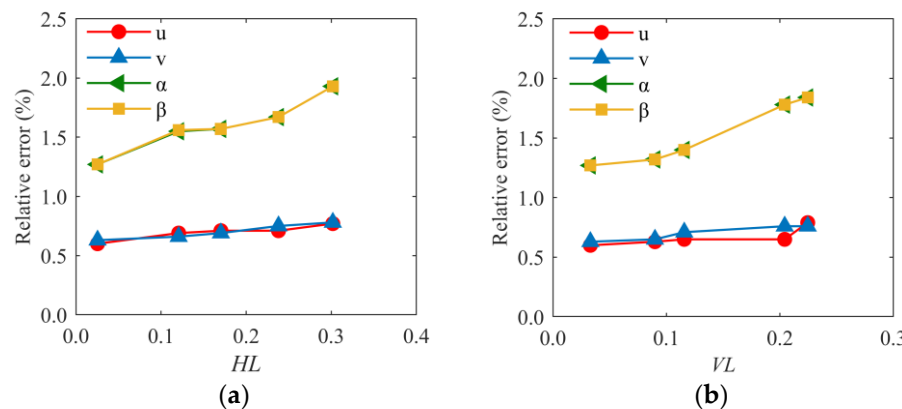


Figure 10. The relationship between the symmetry level of corners in the image and the calibration quality. (a) The horizontal symmetry level; (b) the vertical symmetry level.

(IV) The inclination angle

Based on Figure 4, the inclination angle of the checkerboard pattern in the image is adjusted by changing θ_1 and θ_2 . A series of images with different inclination angles is generated, as shown in Figure 11. Experiments are carried out following the steps described in part (I) of Section 3.3. The rotation angle is taken as the horizontal axis for convenience, and the negative sign represents the direction of rotation.

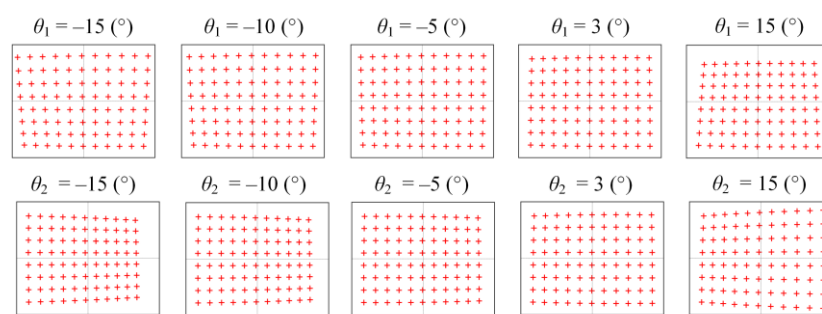


Figure 11. The distribution of corners in images with different inclination angles.

The results shown in Figure 12 indicate that the increase of the rotation angle can decrease E_α and E_β but increase E_μ and E_v . Furthermore, the fluctuations of E_α and E_β are

greater than those of E_μ and E_v with changes in rotation angles. This phenomenon occurs because the change of the inclination angle causes the change of the symmetry level. The effects of the inclination angle and the symmetry level on the accuracy of the focal length and the principal points are different. The effect of the inclination angle on the accuracy of the focal length is more significant than that of the symmetry level. The opposite is true for the principal points. Therefore, we can appropriately increase the rotation angle to improve the calibration quality.

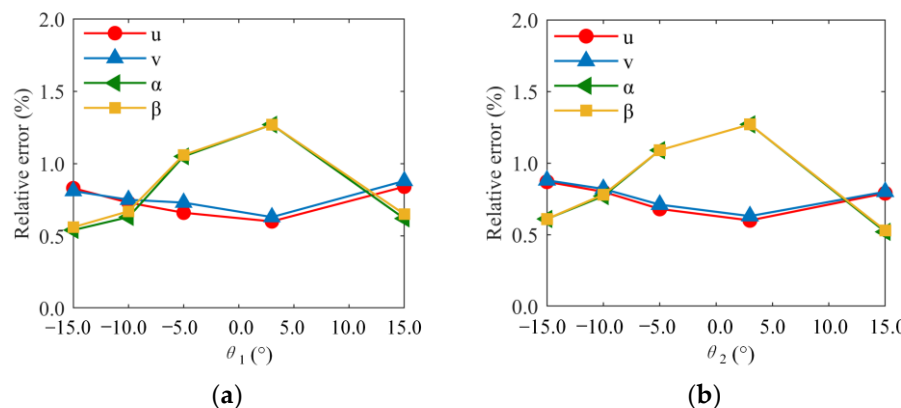


Figure 12. The relationship between the inclination angle of the checkerboard in the image and the calibration quality. (a) The rotation angle of the planar pattern around X_c ; (b) the rotation angle of the planar pattern around Y_c .

According to the above simulated analysis, the guidance during the calibration procedure can be summarized as follows, which can ensure and even improve the calibration quality:

- (i) The number of corners in the image should be as many as possible.
- (ii) The pattern should cover as much of the camera's field of view as possible.
- (iii) The corners in the image should be more symmetrical about the image midline.
- (iv) The inclination angle of the checkerboard in the image can be appropriately large.

4. Experiment and Analysis

The proposed method undergoes testing using both simulated data and real-world images. In these experiments, to evaluate the quality of the calibration method, the mean squared reprojection error (Re) is introduced as an evaluation indicator, defined as follows:

$$Re = \frac{1}{n} \sum_{i=1}^n \sqrt{\|\mathbf{p}_{dij} - \bar{\mathbf{p}}_{dij}\|^2}, \quad (23)$$

where $\bar{\mathbf{p}}_{dij}$ is the reprojection corner, and \mathbf{p}_{dij} is the extracted corner.

4.1. Anti-Noise Performance Test

Calibration from real images involves estimation error due to the existences of sensor noise, digitization error, photon noise, and so on. Therefore, it is important for a high-quality calibration method to be as insensitive to noise as possible. The anti-noise performance of the proposed method is tested and then compared with three advanced and most relevant single-image-based methods, which are Wang's method [18], Huang's method [25], and Genovese's method [26].

In the experiment, simulated corners are generated according to the provided guidance in Section 3.3, as shown in Figure 13. The extrinsic parameters are set as $r = [5^\circ, 5^\circ, 0^\circ]$ and $t = [-155 \text{ mm}, -105 \text{ mm}, 560 \text{ mm}]$. The camera intrinsic parameters, lens distortion parameters, and planar pattern settings match those used in Figure 4. Gaussian noise with

a mean of 0 and a standard deviation varying from 0 to 1 pixel is added to the simulated corners. The experiment is conducted independently 20 times for each noise level using the proposed method, Wang's method, Huang's method, and Genovese's method. Figure 14 shows the simulated results.

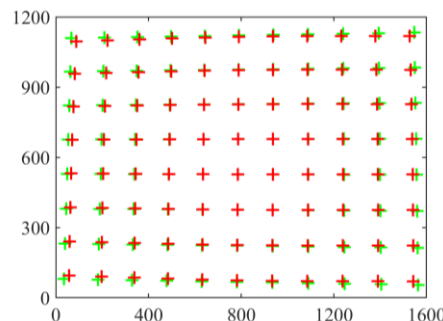


Figure 13. Simulated corners. The green plus sign represents the pixel coordinates of undistorted corners, and the red plus represents the pixel coordinates of distorted corners.

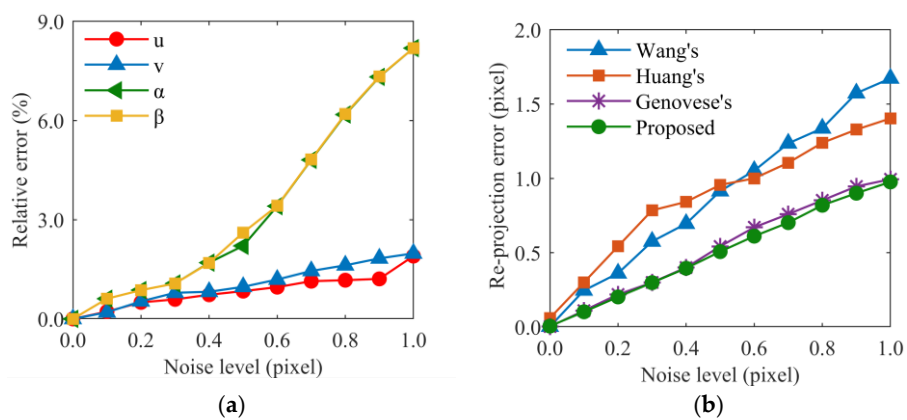


Figure 14. The simulated results. (a) The effects of noise on intrinsic parameters by the proposed method; (b) the effects of noise on Re .

In Figure 14a, E_α , E_β , E_μ , and E_v increase with the growth of noise level. It indicates that the noise affects the accuracy of the proposed method. When Gaussian noise with mean 0 and standard deviation 0.2 pixels is applied, E_μ and E_v are less than 0.7%, and E_α and E_β are less than 1.3%. The results in Figure 14b show that Re in the three methods increases linearly with the increase of noise level, and Re in the proposed method is smaller than that in Huang's method, Wang's method, and Genovese's method at different noise levels. It means that the proposed method has a better anti-noise performance than the other three methods.

4.2. Accuracy Assessment

This part aims to evaluate the accuracy of the proposed method. E_α , E_β , E_μ , E_v , and Re are selected as evaluation indicators, defined in Equations (22) and (23). The calibration results of the well-known multi-image-based Zhang's (WM-Zhang's) method [10] are considered as the reference true values. In addition, Wang's method [18], Zhang's method [15], Huang's method [25], and Genovese's method [26] are selected for comparison, which are advanced and the most relevant.

Real experiments are carried out with an LT-H8179 camera and the planar pattern with 8×11 corners. The image resolution is 1920 pixels \times 1080 pixels, and the pixel size is 2.7 μm . The checkerboard grids are printed uniformly on the plane, with a cell size of 30 mm \times 30 mm. A single image, shown in Figure 15a, is taken. The camera is calibrated using the proposed method, Wang's method, Zhang's method, Huang's method, and Genovese's method. The calibration results are shown in Table 3. Subsequently, fifteen

images are taken, as shown in Figure 15b. The camera calibration results obtained by the fifteen images using WM-Zhang's method are also shown in Table 3. Because of the different distortion models used by the different methods, the positive and negative distortion coefficients estimated by the different methods are different. Given this, it is hard to obtain the relative error of k_1 and k_2 . A comparison of E_α , E_β , E_μ , and E_v of the different methods, shown in Figure 16, is used to evaluate the accuracy of the proposed method.



Figure 15. Images used for calibration experiments. (a) A single image; (b) a set of images.

Table 3. Calibration results of different methods.

| Method | α (Pixel) | β (Pixel) | u (Pixel) | v (Pixel) | k_1 (Pixel $^{-2}$) | k_2 (Pixel $^{-4}$) |
|-----------------|------------------|-----------------|-------------|-------------|------------------------|------------------------|
| Proposed | 1423.4 | 1423.2 | 989.0 | 538.0 | -4.2×10^{-8} | 4.2×10^{-14} |
| Wang's [18] | 1516.9 | 1519.7 | 960.0 | 540.0 | -4.1×10^{-8} | 4.1×10^{-14} |
| Zhang's [15] | 1458.2 | 1458.3 | 983.7 | 548.0 | 4.3×10^{-8} | -4.2×10^{-14} |
| Huang's [25] | 1507.4 | 1507.3 | 975.8 | 546.0 | 4.7×10^{-8} | -4.8×10^{-14} |
| Genovese's [26] | 1378.8 | 1379.0 | 994.4 | 539.8 | 4.3×10^{-8} | -4.1×10^{-14} |
| WM-Zhang's [10] | 1439.4 | 1439.3 | 990.7 | 547.7 | 4.2×10^{-8} | -4.3×10^{-14} |

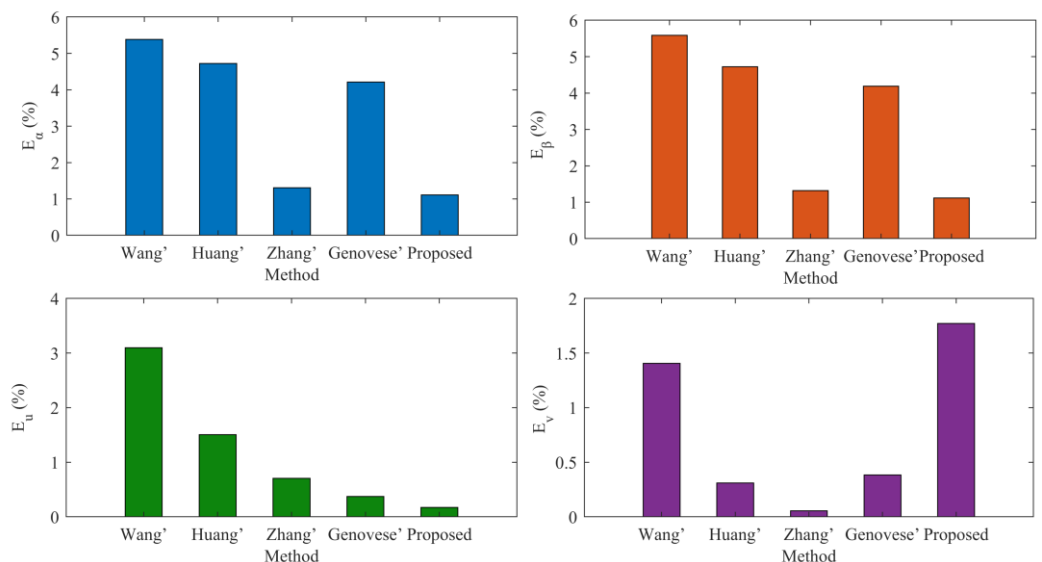


Figure 16. Relative error of calibration results of different methods.

Figure 16 shows that the values of E_α , E_β , E_μ , and E_v for the proposed method are all below 1.8%, indicating that its accuracy is comparable to WM-Zhang's method. Moreover, the values of E_α , E_β , and E_μ for the proposed method are higher than those of the other four methods, demonstrating that the estimation of α , β , and μ using the proposed method is the most accurate. Nevertheless, the value of E_v for the proposed method is smaller than those of the other four methods, suggesting that there is potential for improvement in the calibration accuracy of v . Further observation shows that E_α , E_β , E_μ , and E_v obtained by Wang's method, Zhang's method, Huang's method, and Genovese's method are all less than 5.4%, 1.3%, 4.8%, and 4.2%, respectively. The internal parameter calibration accuracy of the proposed method is 66.7%, 62.5%, and 57.1% superior to that of Wang's method,

Huang's method, and Genovese's method, but is slightly smaller than that of Zhang's method. In fact, a comparison of the calibration accuracy of k_1 and k_2 is not added. It does not mean that the calibration quality of Zhang's method is better than that of the proposed method.

To compare the accuracy of k_1 and k_2 calibrated by the proposed method and the comparison methods, fitting error is introduced as the evaluation indicator. Moreover, another five images, as shown in Figure 17, are taken as the experimental targets, which can make the experimental results more convincing because these images are not involved in the calibration process. The experimental procedures are shown in Figure 18. First, the five images are corrected based on the calibration results presented in Table 3. Then, by Equation (5), the fitting error of each corrected image using each method is calculated, and the results are displayed in Table 4.

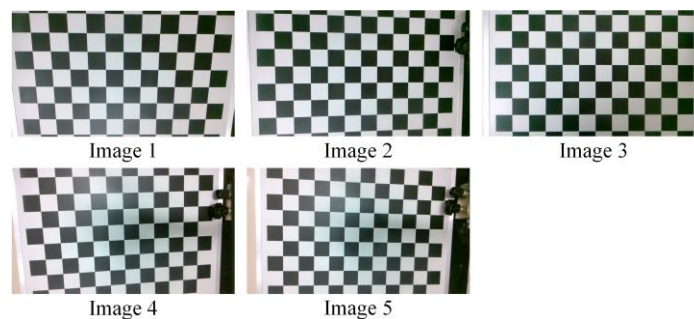


Figure 17. Testing images.

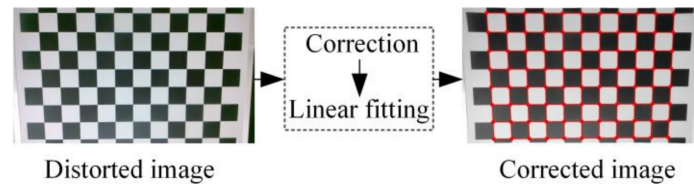


Figure 18. Experimental procedures.

Table 4. The results of the fitting error for the testing images.

| Method | Image 1 (Pixel) | Image 2 (Pixel) | Image 3 (Pixel) | Image 4 (Pixel) | Image 5 (Pixel) |
|-----------------|--------------------|--------------------|--------------------|--------------------|--------------------|
| None | 11.902 | 10.578 | 10.863 | 10.796 | 10.360 |
| Proposed | 5.551 | 3.618 | 3.870 | 3.348 | 3.434 |
| Wang's [18] | 5.660 | 3.989 | 4.170 | 3.534 | 3.754 |
| Zhang's [15] | 5.514 | 3.792 | 4.113 | 3.546 | 3.747 |
| Huang's [25] | 6.958 | 4.058 | 4.351 | 3.834 | 5.622 |
| Genovese's [26] | 6.372 | 3.693 | 3.887 | 3.353 | 3.539 |
| WM-Zhang's [10] | 6.426 | 3.201 | 3.716 | 3.278 | 3.177 |

Table 4 and Figure 19 show the results of the fitting error for the uncorrected images and corrected images. Obviously, the fitting errors of the corrected images are significantly reduced compared with those of the uncorrected images, and the fitting errors of the five images corrected by the proposed method are less than those of the five images corrected by Wang's, Zhang's, Huang's, and Genovese's methods. Thus, it is evident that the proposed method has an excellent performance in distortion correction for images. The proposed method is the most outstanding in the performance of distortion correction among the five methods. That is to say, the accuracy of k_1 and k_2 calibrated by the proposed method is higher than that of k_1 and k_2 calibrated by the comparison methods. Combined with the analytical results in Figure 16, the calibration quality of the proposed method is convincingly higher than that of the comparison methods.

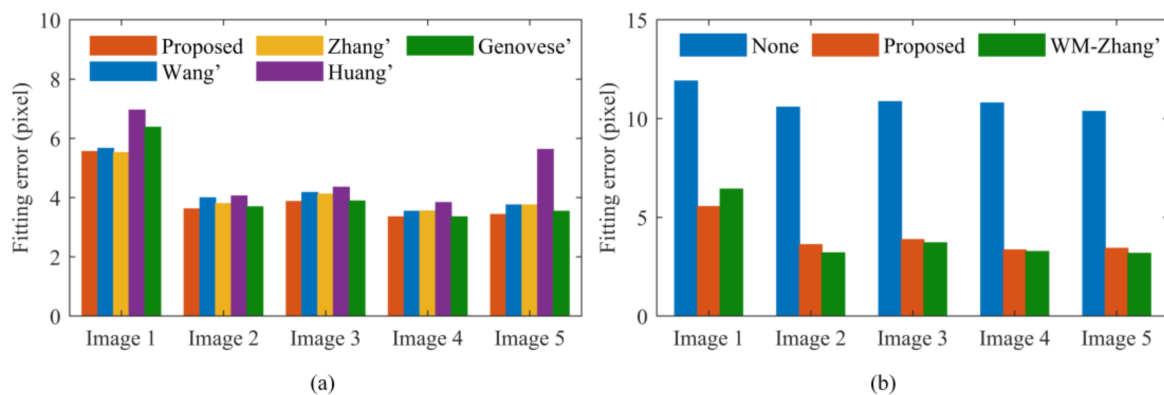


Figure 19. The comparison of the fitting error. (a) The fitting errors of the five images corrected by the proposed method and Wang's, Zhang's, Huang's, and Genovese's methods; (b) the fitting errors of the five images corrected by the proposed method and WM-Zhang's method and those of the five uncorrected images.

In Figure 19a, the fitting errors of Image2, Image 3, Image 4, and Image5 corrected by the proposed method are higher than those of these four images corrected by WM-Zhang's method. The mean fitting error of these four images corrected by WM-Zhang's method is 93.7% of that of the images corrected through the proposed method. However, in Image 1, the fitting error obtained by WM-Zhang's method is higher than that obtained by the proposed method by 19.3%. It is found through Figure 17 that the chessboard of Image 1 fills the field of view most among the five images. Interestingly, the distortion at the edge of the image is generally the largest. Therefore, the proposed method outperforms WM-Zhang's approach in correcting points with significant distortion. Overall, the proposed method shows accuracy in distortion correction that is on par with WM-Zhang's method while being more effective for handling large distortions.

To further assess the calibration quality of the proposed method, reprojection errors of the corners in the five images shown in Figure 17 are calculated. The results are displayed in Table 5 and Figure 20. In Image 1, Re for the proposed method is lower than that of the other five methods, with its error distribution demonstrating the highest degree of concentration. This reinforces the advantages of the proposed method for calibration, as previously mentioned. Additionally, in Images 2–5, both Re and the reprojection error distribution for the proposed method closely align with those of WM-Zhang's method, as opposed to Wang's, Zhang's, Huang's, and Genovese's methods. Furthermore, the average and standard errors of the reprojection error in the five images for the proposed method are lower than those of the comparison methods but slightly higher than those for WM-Zhang's method. Consequently, for the calibration quality, the proposed method is comparable to WM-Zhang's method and better than the comparison methods.

Table 5. The results of Re for the testing images.

| Method | Image 1 (Pixel) | Image 2 (Pixel) | Image 3 (Pixel) | Image 4 (Pixel) | Image 5 (Pixel) |
|-----------------|--------------------|--------------------|--------------------|--------------------|--------------------|
| Proposed | 0.386 | 0.289 | 0.273 | 0.267 | 0.273 |
| Wang's [18] | 0.896 | 0.824 | 0.528 | 0.924 | 0.765 |
| Zhang's [15] | 0.389 | 0.293 | 0.296 | 0.295 | 0.274 |
| Huang's [25] | 0.704 | 0.372 | 0.302 | 0.504 | 0.379 |
| Genovese's [26] | 0.392 | 0.345 | 0.317 | 0.313 | 0.295 |
| WM-Zhang's [10] | 0.403 | 0.252 | 0.267 | 0.222 | 0.228 |

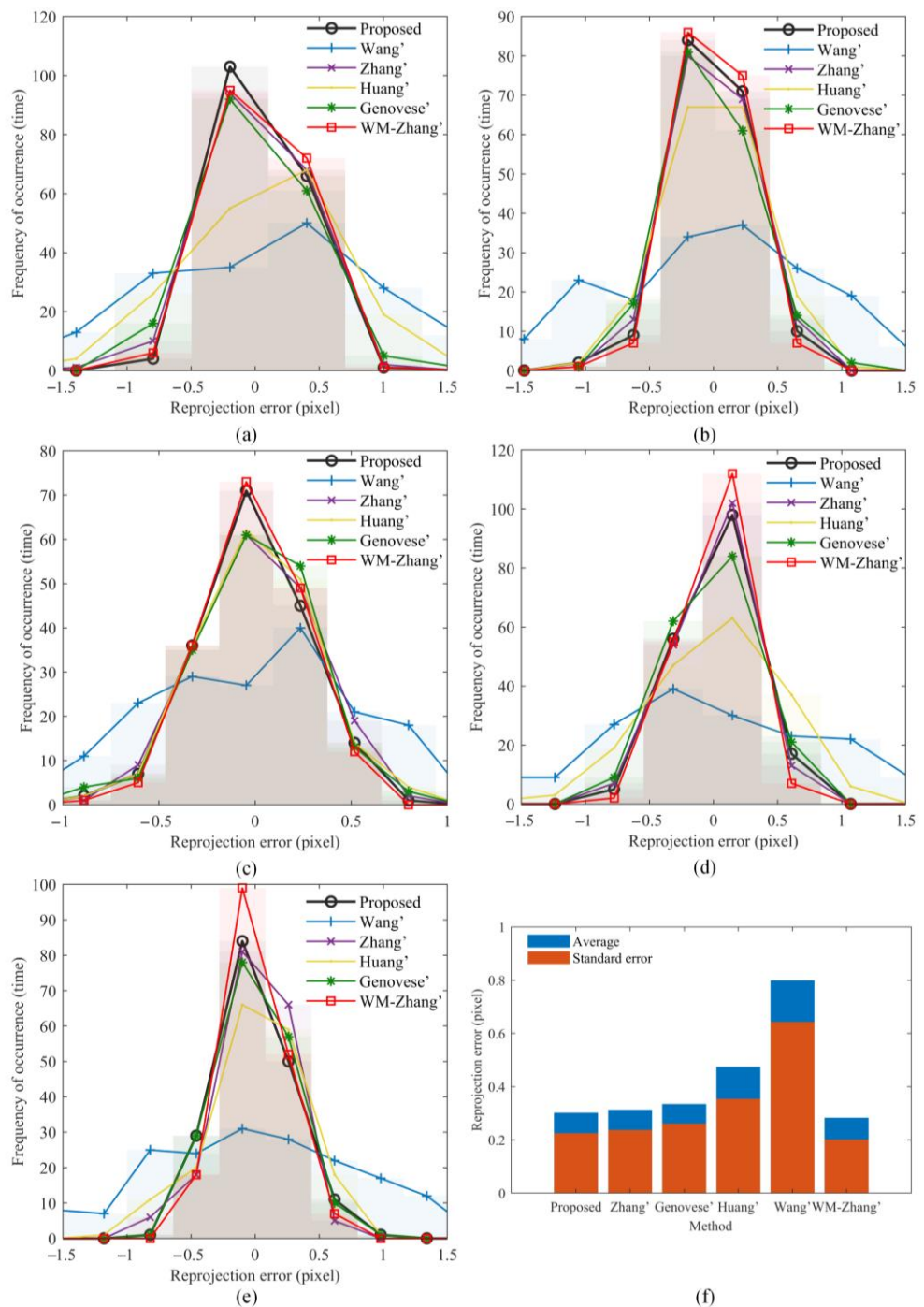


Figure 20. The distribution of the reprojection error of the corners. (a) Image 1, (b) image 2, (c) image 3, (d) image 4, (e) image 5, (f) statistical property.

5. Conclusions

In this paper, the first two radial distortion coefficients and the camera principal points are estimated by minimizing the derived nonlinear objective function using the designed algorithm to correct the distorted corners. Subsequently, the camera focal length and extrinsic parameters are obtained by directly solving linear equations. Additionally, the guidance during the calibration procedure is explored through theoretical analysis and numerical simulation to ensure the calibration quality. It suggests keeping the pattern fully covering the visual field, the corners in the image many and symmetrical about the image midline, and the inclination angle of the pattern in the image appropriately large.

Simulated and real experiments are carried out to test the performance of the proposed method. The experimental results demonstrate that the calibration quality of the proposed method is comparable to that of the well-known multi-image-based Zhang's method [10] and superior to that of the advanced single-image-based methods [20,24,25].

The proposed method provides high-quality camera calibration and excellent distortion correction using only a single image of a commonly used planar checkerboard pattern, which is of high practicability and convenience. However, the algorithm for distortion parameter estimation based on enumeration theory can reach the optimal global solutions at the expense of computation speed. In the future, techniques for saving computation time will be researched to further improve calibration efficiency in applications.

Author Contributions: Methodology, X.X. and H.X.; Software, H.X.; Validation, X.Q. and X.X.; Investigation, X.Q.; Data curation, H.X.; Writing—original draft, X.Q.; Writing—review & editing, X.X.; Visualization, X.Q.; Supervision, X.X.; Funding acquisition, X.X. All authors have read and agreed to the published version of the manuscript.

Funding: National Natural Science Foundation of China [grant number 61901056]; Key Research and Development Program of Shaanxi [grant number 2024GX-YBXM-197]; the Shaanxi Province Qin Chuangyuan Program-Innovative and Entrepreneurial Talents Project [grant number QCYRCXM-2022-352]; the Scientific Research Project of the Department of Transport of Shaanxi Province [grant numbers 23-10X and 24-74K]; Inner Mongolia Science & Technology Plan [grant number 2021GG0330].

Data Availability Statement: The data presented in this study are available on request from the corresponding author. The data are not publicly available due to privacy.

Conflicts of Interest: The authors declare no conflicts of interest.

References

1. Faugeras, O.D.; Toscani, G. The calibration problem for stereo. In Proceedings of the IEEE Computer Society Conference on Computer Vision and Pattern Recognition(CVPR), Miami Beach, FL, USA, 22–26 June 1986; pp. 15–20.
2. Jeung, D.; Jung, K.Y.H.; Lee, H.J.; Hong, J.S. Augmented reality-based surgical guidance for wrist arthroscopy with bone-shift compensation. *Comput. Meth. Programs Biomed.* **2023**, *230*, 107323. [[CrossRef](#)] [[PubMed](#)]
3. Baca, J.G.A.; Jantos, T.; Theuermann, M.; Hamdad, M.A.; Steinbrener, J.; Weiss, S.; Almer, A.; Perko, R. Automated Data Annotation for 6-DoF AI-Based Navigation Algorithm Development. *J. Imaging* **2021**, *7*, 236. [[CrossRef](#)] [[PubMed](#)]
4. Chen, C.; Yu, J.; Gao, N.; Zhang, Z.H. High accuracy 3D calibration method of phase calculation-based fringe projection system by using LCD screen considering refraction error. *Opt. Lasers Eng.* **2020**, *126*, 105870. [[CrossRef](#)]
5. Chai, B.H.; Wei, Z.Z. Stratified camera calibration algorithm based on the calibrating conic. *Opt. Express* **2023**, *31*, 1282–1302. [[CrossRef](#)] [[PubMed](#)]
6. Luhmann, T.; Fraser, C.; Maas, H.G. Sensor modelling and camera calibration for close-range photogrammetry. *ISPRS J. Photogramm. Remote Sens.* **2016**, *115*, 37–46. [[CrossRef](#)]
7. Guan, B.L.; Yu, Y.J.; Su, A.; Shang, Y.; Yu, Q.F. Self-calibration approach to stereo cameras with radial distortion based on epipolar constraint. *Appl. Opt.* **2019**, *58*, 8511–8521. [[CrossRef](#)]
8. Jin, J.; Li, X.F. Efficient camera self-calibration method based on the absolute dual quadric. *J. Opt. Soc. Am. A Opt. Image Sci. Vis.* **2013**, *30*, 287–292. [[CrossRef](#)]
9. Zhang, Z.Y. Camera calibration with one-dimensional objects. *IEEE Trans. Pattern Anal. Mach. Intell.* **2004**, *26*, 892–899. [[CrossRef](#)]
10. Zhang, Z.Y. A flexible new technique for camera calibration. *IEEE Trans. Pattern Anal. Mach. Intell.* **2000**, *22*, 1330–1334. [[CrossRef](#)]
11. Jiang, J.; Zeng, L.C.; Chen, B.; Lu, Y.; Xiong, W. An accurate and flexible technique for camera calibration. *Computing* **2019**, *101*, 1971–1988. [[CrossRef](#)]
12. Yu, J.; Liu, Y.; Zhang, Z.H.; Gao, F.; Gao, N.; Meng, Z.Z.; Jiang, X.Q. High-accuracy camera calibration method based on coded concentric ring center extraction. *Opt. Express* **2022**, *30*, 42454–42469. [[CrossRef](#)] [[PubMed](#)]
13. Tsai, R.Y. A versatile camera calibration technique for high-accuracy 3D machine vision metrology using off-the-shelf TV cameras and lenses. *IEEE J. Robot. Autom.* **1987**, *3*, 323–344. [[CrossRef](#)]
14. Wang, Q.; Yan, C.; Tan, R.X.; Feng, Y.Y.; Sun, Y.; Liu, Y. 3D-CALI: Automatic calibration for camera and LiDAR using 3D checkerboard. *Measurement* **2022**, *203*, 111971. [[CrossRef](#)]
15. Zhang, Y.; Zhao, X.; Qian, D. Learning-Based Distortion Correction and Feature Detection for High Precision and Robust Camera Calibration. *IEEE Robot. Autom. Lett.* **2022**, *7*, 10470–10477. [[CrossRef](#)]
16. Hold-Geoffroy, Y.; Piché-Meunier, D.; Sunkavalli, K.; Bazin, J.-C.; Rameau, F.; Lalonde, J.-F. A Perceptual Measure for Deep Single Image Camera and Lens Calibration. *IEEE Trans. Pattern Anal. Mach. Intell.* **2023**, *45*, 10603–10614. [[CrossRef](#)] [[PubMed](#)]

17. Jeong, M.; Byun, H.; Lee, S. Learning Camera Parameters with Weighted Edge Attention From Single-View Images. *IEEE Access* **2023**, *11*, 16896–16906. [[CrossRef](#)]
18. Wang, J.H.; Shi, F.H.; Zhang, J.; Liu, Y.C. Camera calibration from a single frame of planar pattern. In Proceedings of the 8th International Conference on Advanced Concepts for Intelligent Vision Systems, Antwerp, Belgium, 18–21 September 2006; pp. 576–587.
19. Zhou, F.Q.; Cui, Y.; Gao, H.; Wang, Y.X. Line-based camera calibration with lens distortion correction from a single image. *Opt. Lasers Eng.* **2013**, *51*, 1332–1343. [[CrossRef](#)]
20. Zhang, Z.; Zhao, R.J.; Liu, E.H.; Yan, K.; Ma, Y.B. A single-image linear calibration method for camera. *Measurement* **2018**, *130*, 298–305. [[CrossRef](#)]
21. Miyagawa, I.; Arai, H.; Koike, H. Simple camera calibration from a single image using five points on two orthogonal 1-D objects. *IEEE Trans. Image Process.* **2010**, *19*, 1528–1538. [[CrossRef](#)]
22. Chen, H.T. Geometry-Based Camera Calibration Using Five-Point Correspondences From a Single Image. *IEEE Trans. Circuits Syst. Video Technol.* **2017**, *27*, 2555–2566. [[CrossRef](#)]
23. Ardakani, H.K.; Mousavinia, A.; Safaei, F. Four points: One-pass geometrical camera calibration algorithm. *Vis. Comput.* **2019**, *36*, 413–424. [[CrossRef](#)]
24. Lee, J.Y. Robust Camera Calibration with a Single Image by Planar Homography. In Proceedings of the 18th IEEE International Conference on Advanced Video and Signal Based Surveillance (AVSS), Madrid, Spain, 29 November–2 December 2022; pp. 1–7.
25. Huang, B.; Zou, S.P. A New Camera Calibration Technique for Serious Distortion. *Processes* **2022**, *10*, 488. [[CrossRef](#)]
26. Genovese, K. Single-image camera calibration with model-free distortion correction. *Opt. Lasers Eng.* **2024**, *181*, 108348. [[CrossRef](#)]
27. Ricolfe-Viala, C.; Sanchez-Salmeron, A.J. Camera calibration under optimal conditions. *Opt. Express* **2011**, *19*, 10769–10775. [[CrossRef](#)]

Disclaimer/Publisher’s Note: The statements, opinions and data contained in all publications are solely those of the individual author(s) and contributor(s) and not of MDPI and/or the editor(s). MDPI and/or the editor(s) disclaim responsibility for any injury to people or property resulting from any ideas, methods, instructions or products referred to in the content.